Separation of Radiances from a Cirrus Layer and Broken Cumulus Clouds in Multispectral Images

Igor Yanovsky and Anthony B. Davis

***Abstract*—In this paper, we introduce methodology for separating layers of reflective surfaces in Earth remote sensing data. We propose a single-channel layer separation framework and extend it to multispectral layer separation. Efficient alternating minimization and fast operator-splitting methods are used to solve minimization problems. Specifically, we apply our methodology to separate strongly stratified and optically thin upper (cirrus) clouds from optically thick lower convective (cumulus) clouds in atmospheric imagery approximated as additive contributions to the observed signal. After setting up synthetic "truth" scenarios, we evaluate the accuracy of the two-layer separation results while varying the effective opaqueness of each of two types of cloud. We show that multispectral cloud layer separation is consistently more accurate than channel-by-channel cloud layer separation.**

***Index Terms*—Cloud layer separation, scale separation, image decomposition, total variation minimization, multispectral image analysis, passive atmospheric tomography**

I. Introduction

CLOUDS are natural part of the Earth's climate system and play a crucial role in its radiative balance. So much so that even small changes in cloud properties that just may be caused by anthropogenic aerosol emissions (i.e., pollution) is a major concern for climate scientists; these are the so-called aerosol indirect impacts on climate, as several varieties have been identified [1]–[3]. Moreover, clouds may be reacting already to other changes in the climate system such as global warming; these are the so-called cloud feedbacks on climate [4], [5]. Indirect aerosol effects and cloud feedbacks have been identified as major sources of uncertainty in forecasting future climate due to our poor understanding of them [6].

This situation creates a challenge for climate modelers, and cloud remote sensing scientists as well. Can the latter not better exploit the massive amounts of satellite data on clouds and shed new light on these critical cloud-related issues in climate science? Along with a small team of scientists at JPL and collaborators elsewhere, the present authors have picked up this challenge and, collectively, we are revisiting the fundamentals of passive cloud and aerosol remote sensing in the visible and near-IR (VNIR) spectrum, framing it as a problem in atmospheric tomography. This initiative is dubbed the "Three-Dimensional Tomographic Reconstruction of the Aerosol-Cloud Environment" (3D-TRACE).

I. Yanovsky (corresponding author) and A.B. Davis are with the Jet Propulsion Laboratory, California Institute of Technology, Pasadena, CA 91109 USA and the University of California, Los Angeles, Joint Institute for Regional Earth System Science and Engineering, Los Angeles, CA 90095 USA, e-mail: igor.yanovsky@jpl.nasa.gov.

Manuscript received March 19, 2014; revised March 19, 2014.

The main source of information we have on airborne particles is from radiation in the solar spectrum scattered toward sensors in space, on aircraft or ground-based. 3D-TRACE is predicated largely on a new class of multi-pixel/multi-angle retrieval methods applied to reflected solar light. This is a radical departure from the state-of-the-art in passive remote sensing of atmospheric particulates, either densely aggregated in clouds or aerosol plumes or dispersed into the background aerosol. Indeed, at present, the processing of the raw (radiance) data into geophysical "products" is performed operationally on a pixel-by-pixel basis, often with a single viewing angle.

Working at the pixel scale and ignoring the spatial context justifies the use of so-called "1D" radiative transfer [7] as a forward model in the inverse problem of inferring from measured radiances the inherent optical, microphysical and chemical properties of the particles. 1D RT ignores explicitly all net horizontal transport of radiation driven by horizontal gradients in atmospheric or surface properties. In contrast, the use of 1D RT in the thermal through microwave spectral region is more justified since scattering is truly secondary to emission and absorption, and has frequently been used to deliver vertical profiles. In most of the solar spectrum however, there is little sensitivity to the height of the scattering particles in the atmosphere,[1] inasmuch as it is well defined. Consequently, between the muddling of horizontal variability in 1D RT and the insensitivity of scattered light to stratification and the frequent utilization of a single view, aerosol and cloud retrievals can only target column-integrated quantities such as optical thickness. For vertical profiles, one traditionally needs active instruments: lidars for aerosols, mm-wave radars for clouds. But then, from space at least, the vertical information is only available along the "curtain" defined by the sub-satellite transect.

3D-TRACE takes a resolutely 3D RT, multi-angle and multi-pixel approach to extend this profiling capability horizontally using passive imagers with broad swaths. It is an ambitious program that has to start with small steps to establish its overall feasibility. From the outset, 3D-TRACE does not look at satellite imagery as a collection of cloudy and clear pixels to be processed respectively and independently into either cloud or aerosol products. It does recognize however that atmospheric tomography will proceed differently in optically thick and thin regions, that is, opaque highly reflective clouds or dense aerosol plumes near sources (biomass burning, volcanoes, etc.) on the one hand, and tenuous aerosol plumes at significant

[1]The exception to this rule is deep blue and near-UV because of Rayleigh scattering and oxygen bands because of the differential absorption.

distances from sources or elevated optically thin cirrus clouds on the other hand.

A necessary ingredient of an atmospheric tomography framework is therefore the ability to separate, not horizontally (as in clear vs. cloudy pixels), but vertically two cloud layers. A frequently observed superposition of cloud layers is indeed an elevated semi-transparent cirrus (Ci, made of ice crystals) through which one can clearly see a low-level layer of broken cumulus clouds (Cu, made of water droplets).

The purely spectral (pixel-by-pixel) solution to this particular cloud layer separation problem is to use a strong water vapor absorption feature such as its $\sim$1.38 μm band [8], [9]. A 1.38 μm "cirrus" channel indeed reveals in back-scattered light only what is above the well-mixed boundary layer that contains most of the humidity. In short, any Ci layer that may be present in the upper troposphere will appear in the 1.38 μm channel. That channel however may not always be available and, moreover, the conditions for it to work are not always realized. For instance, the surface and any low-level clouds that may be present are clearly visible at 1.38 μm if humidity happens to be low, and there are dry regions where this is almost always the case.

The question therefore remains: Can we separate the Ci and the broken Cu clouds using only spatial properties? Cirrus clouds have relatively smooth variability in space often with relatively low amplitude. In sharp contrast, the cumulus clouds are optically thick, hence bright, with relatively sharp boundaries. Can we separate, on that basis alone, the radiances contributed by the Ci and the Cu clouds?

First, we note that this cloud layer separation problem is important in its own right. Apart from the rationale for atmospheric tomography, which is largely based on climate modeling needs, there are other applications: weather, agriculture, solar energy, surveillance, defense, and so on. Clouds affect visibility and are entangled dynamically with turbulence. Turbulence that develops in convective clouds affects aircraft. The list goes on.

In mathematical lingo, the "slow" variation in space characteristic of elevated cirrus layers is called "low oscillatory" behavior. In contrast, the lower convective clouds are bright (due to their large optical thickness) and have relatively sharp boundaries. They are either "high oscillatory" or prominently occupy large contiguous areas. Due to their inherent brightness, the lower convective clouds optically overwhelm the upper clouds (cf. panel (a) in Fig. 2).

Given multispectral images in VNIR spectrum, our goal is to solve the cloud layer separation problem, or decomposition of images into contributions from high-oscillatory lower convective clouds and low-oscillatory upper cirrus clouds. Multilayer separation is conceptually similar to image decomposition and segmentation problems. Decomposition of images into a piecewise smooth component (cartoon) and high-oscillatory component (texture) has been a rapidly developing field in recent years. A variety of proposed total variation-based methods for image decomposition rely on different metrics for modeling textures [10]–[18]. Models for image segmentation, many of which are variational methods [19]–[21], have also been effective for solving other types of classification problems in many applications.

Unlike in image decomposition and segmentation applications, however, a given area (or a pixel) in a manifestly two-layered cloud image may be a part of one, none, or both layers. Another challenge that distinguishes the layer separation problem is the fact that one of the layers may obstruct another layer in large parts of an image, thus blocking features in an obstructed layer. An application considering multiple layers of clouds is an example where such challenges occur.

In this paper, we solve layer separation problem within the energy minimization framework. We introduce a methodology for single-channel layer separation and generalize it to multichannel framework. Our formulations are related to problems that arise frequently in compressed sensing [22], [23]. The energy functionals are minimized using efficient operator-splitting methods.

There is a rich source of multi-angle multispectral data, containing a wide variety of scenes, which is available to test our methodology. The data is acquired by the Multi-angle Imaging Spectro-Radiometer (MISR), which has nine digital cameras, pointing at different angles, and gathering data in four different spectral bands of the visible spectrum [24]. Each region on Earth's surface is successively captured by all nine cameras in blue, green, red, and near-IR wavelengths as the Terra satellite (carrying MISR) overflies it.

The structure of the paper is follows. Section II introduces notations used throughout the paper. The multilayer separation model for single-channel images is introduced in Section III, with more details provided in Appendix A. Section IV proposes the multilayer separation model for multichannel images and is supplemented by Appendix B. Results are discussed in Section V. We conclude the paper in Section VI, and discuss future work.

II. Notation

We first introduce notations that will be used throughout the paper. Let Ω be an image domain, $\Omega \subset \mathbb{R}^n$. In this paper, we assume we are working with two-dimensional images: $n = 2$.

For a *single-valued function* (single-channel image) $u : \Omega \subset \mathbb{R}^2 \to \mathbb{R}$, we use the following notations to define the norms:

$$||u||_1 = \sum_{(i,j)\in\Omega} |u_{ij}|, \qquad ||u||_2 = \sqrt{\sum_{(i,j)\in\Omega} |u_{ij}|^2}.$$

The gradient of u is denoted as ∇u, with $\nabla u \in \mathbb{R}^2$. For a vector-valued function $\mathbf{d} = (d_1, d_2) \in \mathbb{R}^2$, for example $\mathbf{d} = \nabla u$, the norms are defined as

$$||\mathbf{d}||_1 = \sum_{(i,j)\in\Omega} ||\mathbf{d}_{ij}||_2, \qquad ||\mathbf{d}||_2 = \sqrt{\sum_{(i,j)\in\Omega} ||\mathbf{d}_{ij}||_2^2}, \quad (1)$$

where $||\mathbf{d}_{ij}||_2 = \sqrt{(d_1)_{ij}^2 + (d_2)_{ij}^2}$.

For a *vector-valued function* $\mathbf{u} : \Omega \subset \mathbb{R}^2 \to \mathbb{R}^C$, representing a multichannel image $\mathbf{u} = (u^{(1)}, u^{(2)}, \ldots, u^{(C)})$,

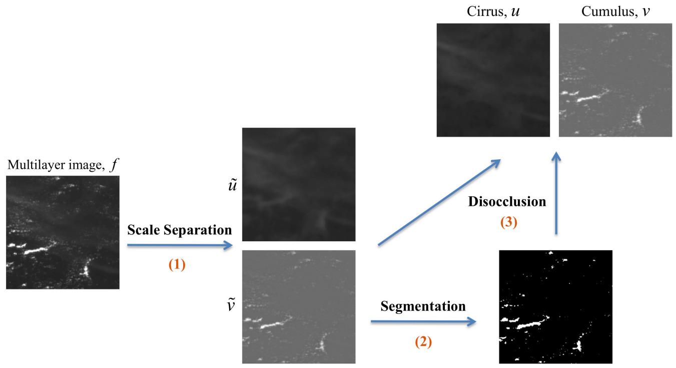

Fig. 1. Diagram of Algorithm 1. Scale separation of image f is performed to obtain a rough estimate of cirrus $\tilde{u}$ and cumulus $\tilde{v}$ layers. Segmentation of cumulus layer estimate finds regions for disocclusion.

where C is the number of channels in an image, we use the following notations to define the norms:

$$||\mathbf{u}||_1 = \sum_{(i,j)\in\Omega} \left(|u_{ij}^{(1)}| + \ldots + |u_{ij}^{(C)}| \right),$$

$$||\mathbf{u}||_2 = \sqrt{\sum_{(i,j)\in\Omega} (u_{ij}^{(1)})^2 + \ldots + (u_{ij}^{(C)})^2}.$$

We denote the generalization of the gradient for vector-valued function $\mathbf{u}$ as $\nabla\mathbf{u} \in \mathbb{R}^{2C}$. For $\mathbf{d} = \nabla\mathbf{u}$, the norms are defined as in (1), with $||\mathbf{d}_{ij}||_2 = \sqrt{(d_1)_{ij}^2 + \ldots + (d_{2C})_{ij}^2}$.

Unless specified otherwise, $||\cdot|| = ||\cdot||_2$ in the remainder of the paper.

III. Multilayer Separation of Single-Channel Images

Let f represent an observed single-channel image containing multiple layers. We propose a general variational framework for decomposition of image f into images u and v containing the two layers. Image u will contain a low-oscillatory layer, and image $v = f - u$ will have a layer that prominently occupies large contiguous areas and obstructs, or optically overwhelms, the low oscillatory layer. We denote by D, with boundary ∂D, the (usually disjoint) region where possible obstruction occurs. We consider the following energy minimization problem for scale separation:

$$\min_{\tilde{u}} \; \{ \, R(\tilde{u}) + \mu ||f - \tilde{u}||_* \, \}, \tag{2}$$

where $R(u)$ is the regularization term, which puts a penalty on high-oscillatory components. The term $||f-u||_*$ models high-oscillatory components. Examples of these terms are listed in Appendix A. Parameter μ is nonnegative.

Scale separation minimization (2) generates only a rough estimate of multilayer separation. As seen on Fig. 1, there are traces of cumulus clouds in the image containing cirrus layer, that is, $\tilde{u}$. We note that such irregularities occur in regions where optically thick lower convective clouds occupy large contiguous areas in the image. In order to recover a more accurate representation of u (and, therefore, v), we perform disocclusion in these regions. To find such regions D or, equivalently, to determine region boundaries ∂D, we perform segmentation of image $\tilde{v} = f - \tilde{u}$, containing the high-oscillatory layer. The following disocclusion minimization problem is subsequently solved:

$$\begin{cases} \min\limits_{u} \; R(u) & \text{in } D, \\ u = \tilde{u} & \text{in } \Omega \backslash D, \end{cases} \tag{3}$$

with $u_0 = \tilde{u}$ as initial conditions and Neumann boundary conditions on D.

Algorithm 1 below is a high level description of the proposed cloud layer separation process. Figure 1 shows a graphical diagram displaying steps in Algorithm 1. Appendix A describes each step of Algorithm 1 in greater detail.

Algorithm 1 Cloud Layer Separation

1: Given multilayer image f, solve scale separation subproblem (2) to obtain preliminary $\tilde{u}$ and $\tilde{v}$, such that $f = \tilde{u}+\tilde{v}$.
2: Perform segmentation of image $\tilde{v}$ from Step 1 in order to determine (usually disjoint) region D.
3: Solve disocclusion problem (3) in region D in order to find more accurate layers u and v, such that $f = u + v$.

IV. Multilayer Separation of Multichannel Images

In this section, we extend the multilayer separation framework, introduced in Section III, to multichannel images. The observed multichannel image is denoted as $\mathbf{f} = (f^{(1)}, f^{(2)}, \ldots, f^{(C)})$, and it is decomposed into two layers, $\mathbf{u}$ and $\mathbf{v}$. Similar to a single-channel case (2, 3), the energy minimization problems for multichannel scale separation and disocclusion we consider are:

$$\min_{\tilde{\mathbf{u}}} \; \{ \, R(\tilde{\mathbf{u}}) + \mu ||\mathbf{f} - \tilde{\mathbf{u}}||_* \, \}, \tag{4}$$

and

$$\begin{cases} \min\limits_{\mathbf{u}} \; R(\mathbf{u}) & \text{in } D, \\ \mathbf{u} = \tilde{\mathbf{u}} & \text{in } \Omega \backslash D, \end{cases} \tag{5}$$

respectively.

Appendix B gives more details on the proposed implementation of multichannel cloud layer separation. In the following analyses, we use data acquired by MISR in four different spectral bands: near-infrared (N), red (R), green (G), and blue (B), by decreasing wavelength. An observed multichannel MISR image containing two cloud layers can therefore be represented as $\mathbf{f} = (f^{(\mathrm{N})}, f^{(\mathrm{R})}, f^{(\mathrm{G})}, f^{(\mathrm{B})})$.

V. Results

In our experiments, we used MISR data acquired with nine digital push-broom cameras, pointing at different angles and gathering radiance measurements in four different spectral bands in the solar spectrum. Each region on Earth's surface is successively captured by all nine cameras in blue, green, red, and near-infrared wavelengths as the Terra platform overflies it.

The data used in this paper were a real multichannel image (Fig. 3(a)) and a grayscale version of the same image

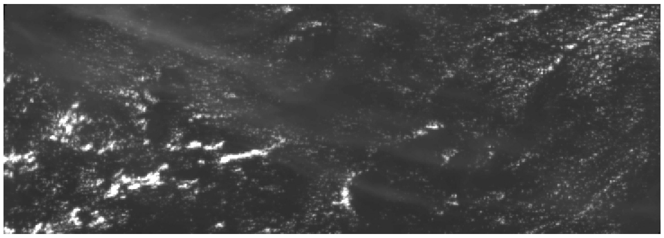

(a) Grayscale double-layer cloud image

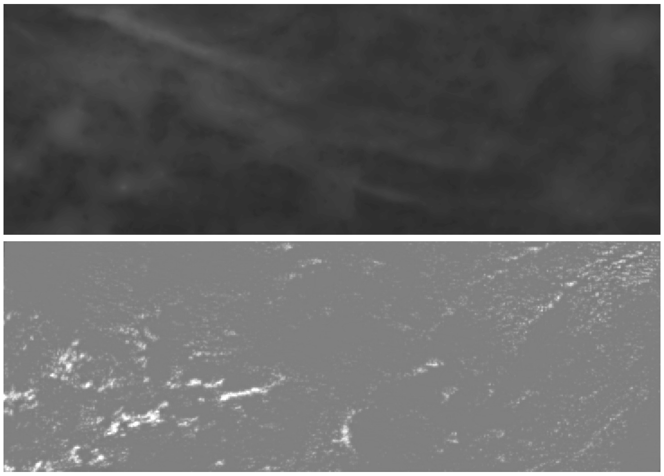

(b) Cloud layer separation

Fig. 2. Grayscale (single-channel) layer separation. (a) Grayscale double-layer cloud image from MISR [24] with an optically thin high-level cirrus layer over a low-level field of broken cumulus. (b) Top and bottom panels show the reconstructed cirrus and cumulus layers, respectively, after single-channel layer separation was performed.

(Fig. 2(a)). We also generated synthetically a series of multichannel images by adding nearly-pure cirrus and cumulus layers while varying opaqueness of each of two types of clouds (Fig. 5). This provides us with "ground truth" scenarios where the accuracy of multilayer separation results can be easily evaluated.

Throughout this paper, we consistently used the same set of parameters for all multichannel experiments. These parameters are listed in the appendices.

In this section, we show cloud layer separation results for single-channel and multichannel images, as well as compare channel-by-channel and multichannel cloud layer separation results for various thicknesses of cirrus and cumulus clouds. *Channel-by-channel layer separation* is performed using single-channel separation on each of the four channels as described in Section III and Appendix A. *Multichannel layer separation* is performed using the process described in Section IV and Appendix B.

A. Demo with an actual MISR image

We first consider a 1460x512 single-channel multilayer image shown on Fig. 2(a). This image was generated by combining all four MISR channels of a real image to create a grayscale image. As is noticeable on this image, the upper cirrus clouds vary slowly in space and are optically thin. By contrast, the lower convective clouds are optically thick, have relatively sharp boundaries, and optically overwhelm the upper clouds. Fig. 2 shows results obtained after decomposing this image into low-oscillatory cirrus layer, u (Fig. 2(b), top), and optically thick convective cloud layer, v (Fig. 2(b), bottom).

We next consider a multichannel image on Fig. 3(a). Figure 3(b) shows low-oscillatory cirrus layer, $\mathbf{u}$, and lower optically thick convective clouds, $\mathbf{v}$, as obtained using channel-by-channel layer separation. Figure 3(c) shows multichannel layer separation results. Compared to channel-by-channel layer separation (Fig. 3(b)), multichannel cloud layer separation result is visibly more accurate, in particular, with less artifacts present in cirrus layer. We note that color images in Fig. 3 depict red, green, and blue channels in "true color," while layer separation was performed on all four channels.

B. Error quantification with synthetic MISR images

We generated up a sequence of synthetic multichannel images where truth is known. To accomplish this, we chose two distinct scenes (678x420 images), shown on Fig. 4(a,b), one containing only optically thin cirrus clouds and the other containing only convective cumulus clouds. We denote by $\mathbf{u}^{(t)}$ and $\mathbf{v}^{(t)}$ the images containing cirrus and cumulus clouds, respectively. The weighted sum of these two single-layer images is a two-layer image for which we know the truth.

Note that color images from Fig. 4 on are displayed as near-infrared (R), red (G), and green (B), i.e., the standard "false color" rendering. Layer separation was performed of course on all four channels.

We expect the performance of cloud layer separation methods to vary as the relative opacity of cirrus layer changes relative to that of the cumulus layer. In order to construct two-layer images with layers of various relative opacities, we vary the respective brightnesses of cirrus and cumulus clouds using nonnegative opaqueness coefficients, ci and cu, respectively. We generate images $\mathbf{f}$ that satisfy

$$\begin{aligned} &\mathbf{f} = ci \cdot \mathbf{u}^{(t)} + cu \cdot \mathbf{v}^{(t)}, \quad \text{such that} \\ &\max_{(i,j)\in\Omega} \{ci \cdot \mathbf{u}^{(t)} + cu \cdot \mathbf{v}^{(t)}\} = constant. \end{aligned} \tag{6}$$

As opaqueness coefficients vary, the maximum of weighted sum in (6) equals to the same $constant$. Smaller ci/cu ratio indicates the relative optical thinness of cirrus clouds, and prominence of cumulus clouds. In contrast, larger ci/cu ratio indicates increased optical thickness of the cirrus layer. In this case, cirrus clouds become as optically thick as cumulus clouds, making the layers indistinguishable and negatively affecting the accuracy of cloud layer separation.

We performed thirteen experiments, with ci ranging from 0 to 2.6, and cu from 1.04 to 0. Accordingly, ci/cu ratio ranges from 0 to ∞. Figure 5 shows three of these scenarios, where $ci/cu = 0.829, 2.345, 6.571$. The three synthetic images are displayed in the top row, with increasing ci/cu from left to right. The next two rows show respectively the true and the retrieved cirrus. The last two rows echo these ones but for the cumulus layer. The *multichannel* cloud layer separation algorithm was used in all cases. Layer separation results for smaller ci/cu ratios are visibly more accurate (two leftmost columns in Fig. 5), with the cirrus clouds virtually not present in the retrieved cumulus layer image. However,

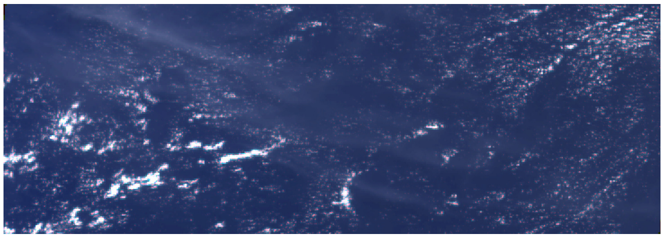

(a) Multichannel double-layer cloud image

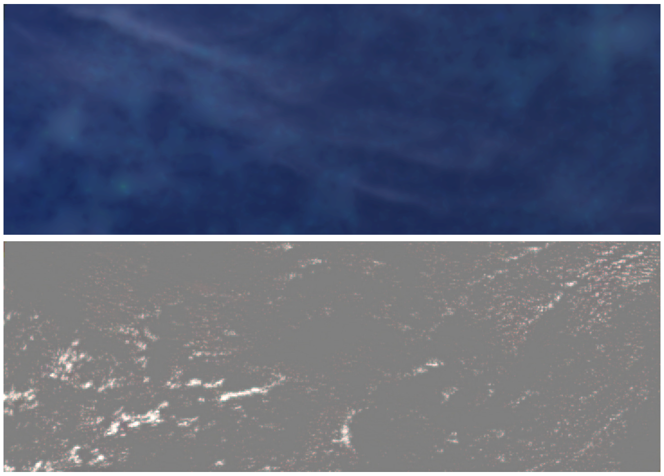

(b) Channel-by-channel layer separation

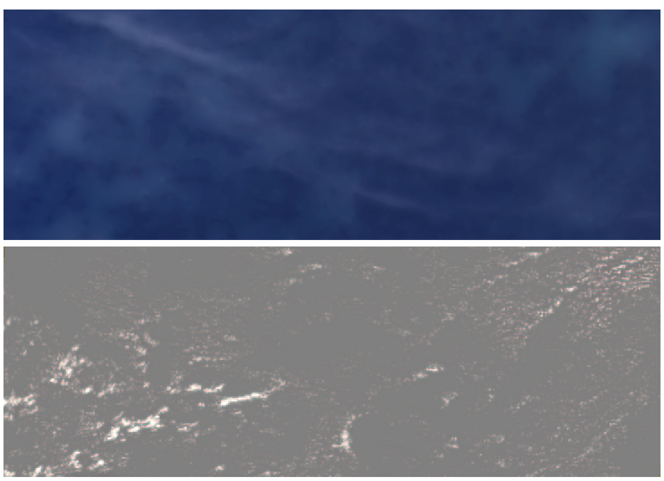

(c) Multichannel layer separation

Fig. 3. Channel-by-channel and multichannel layer separation. (a) Multichannel double-layer cloud image from MISR with an optically thin high-level cirrus layer over a low-level field of broken cumulus. Grayscale image of the same scene is shown in Fig. 2(a). The reconstructed cirrus and cumulus layers are shown after (b) channel-by-channel and (c) multichannel layer separations were performed.

our algorithm is not as accurate for large values of ci/cu, with some cirrus clouds easily seen in computed cumulus layer (rightmost column in Fig. 5). As expected, when cirrus clouds become optically thick ($ci/cu \to \infty$), commensurate with the cumulus clouds, and therefore overwhelming them in the original image, accurate layer separation becomes unfeasible.

Figure 6 shows the truth, the separations and the associated errors in computed cirrus and cumulus layers for the case when $ci/cu = 3.704$, with cirrus on the left and cumulus on the right. The original synthetic image is displayed on Fig. 4(c). The truth is in the top row of Fig. 6. The next row down (b) shows the *channel-by-channel* decomposition followed by the *signed* error fields (c), which are defined as the estimated low and high oscillatory components minus the corresponding truth. For the RGB display, errors are offset so that zero error across all three (R,G,B) channels is mapped to the dominant grey tone, and the error is multiplied by 5 and displayed on the same 0-to-255 scale as used in the first two rows (and elsewhere). Negative errors, and there are few of them, have darker tones and hues. Positive errors are brighter. We immediately see that the error in the cirrus retrieval is essentially a smoothed version of the cumulus field: most identifiable clusters of clouds are present. Conversely, the error in the cumulus retrieval is in essence a sharpened version of the cirrus field: the two dominant streaks are clearly visible. This "cross-talk" between the cirrus and cumulus "channels" is not surprising. The two last rows (d,e) in Fig. 6 echo the 2nd and 3rd but for the *multichannel* cloud layer separation. Overall, the patterns and trends in the error fields are as previously described. Upon closer examination, we see that cirrus-side errors are slightly reduced and that cumulus-side errors are more spectrally neutral (less color is revealed). This is also a natural consequence of pooling all channels in the minimization procedures.

We computed root-mean-square (RMS) errors, errors in L_1-norm, and errors in H_1-norm for all thirteen ci/cu ratios. Given the ground truth $\mathbf{u}^{(t)}$ and the error $\mathbf{e} = \mathbf{u} - \mathbf{u}^{(t)}$, the error norms are computed as

$$\begin{aligned}
\mathbf{e}_{RMS} &= \sqrt{\frac{1}{CN}\sum_{c}\sum_{(i,j)\in\Omega}|e_{ij}^{(c)}|^2}, \\
||\mathbf{e}||_{L_1} &= \frac{1}{CN}\sum_{c}\sum_{(i,j)\in\Omega}|e_{ij}^{(c)}|, \\
||\mathbf{e}||_{H_1} &= \frac{1}{CN}\sum_{c}\sum_{(i,j)\in\Omega}|\nabla e_{ij}^{(c)}|^2,
\end{aligned}$$

where the summation is done over all N pixels in an image and all $c = 1, 2, \ldots, C$ channels. Figure 7 shows plots of error norms for $ci/cu < \infty$. We see that the errors are smaller for smaller ci/cu ratios and increase with increasing opaqueness of cirrus clouds. The errors in multichannel cloud layer separation result are consistently smaller than those in channel-by-channel cloud layer separation. In order to interpret numerical values of errors as displayed on the vertical axis of plots of Fig. 7, it is important to consider that the synthetic images were scaled to be between 0 and 255 ($constant = 255$ in Eq. (6)).

For the case of $ci/cu = 3.704$ (Figure 6), errors in L_1 norm are 1.46 and 1.35 for channel-by-channel and multichannel methods, respectively. Table I shows minimum and maximum values of radiances for true cirrus and cumulus layers for this case. That means, for instance, that relative errors $(100\times)||\mathbf{e}||_{L_1}/|\max - \min|$ are 2.54% and 2.35% for cirrus reconstructions in channel-by-channel and multichannel cases, respectively. The corresponding errors for cumulus reconstructions are 1.47% and 1.36%. Since $f = u + v$ by construction, the error in u would be equal to error in v.

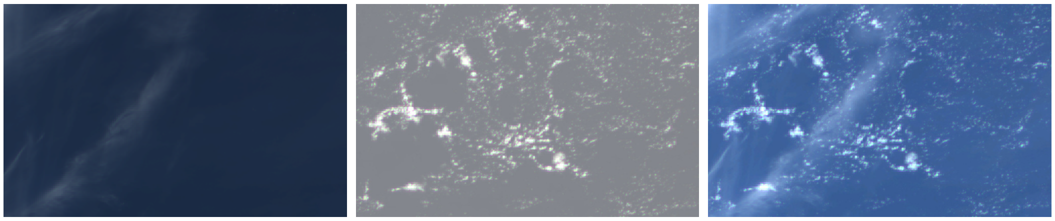

(a) Cirrus clouds, $\mathbf{u}^{(t)}$ (b) Cumulus clouds, $\mathbf{v}^{(t)}$ (c) Synthetic image, $\mathbf{f}$

Fig. 4. Real images containing only (a) cirrus and (b) cumulus clouds. (c) Resulting synthetic image, $\mathbf{f} = ci \cdot \mathbf{u}^{(t)} + cu \cdot \mathbf{v}^{(t)}$, where $ci = 2.0$, $cu = 0.540$, and $ci/cu = 3.704$.

TABLE I
MINIMUM AND MAXIMUM RADIANCE VALUES FOR THE FOUR CHANNELS FOR CIRRUS AND CUMULUS LAYERS IN FIGURE 6(A)

Channels	N	R	G	B
Cirrus [min,max]	[26, 84]	[40, 100]	[66, 122]	[140, 196]
Cumulus [min,max]	[1.6, 107]	[3.2, 132]	[6.5 94]	[18, 93]

C]umulus reconstructions are therefore almost twice as good by this metric, due to their significantly larger range.

We also assessed computational efficiency of the cloud layer separation framework when using fast operator splitting and alternating minimization methods for minimizing energy functionals (see Appendix A). Alternatively, a standard way of minimizing energy functionals such as (7) and (12) is to use gradient descent methods. We found that solving the cloud separation problem using alternate minimization methods is about $8\times$ faster than using gradient descent methods.

VI. CONCLUSION AND FUTURE WORK

We introduced single-channel layer separation framework and extended it to multichannel layer separation. Specifically, we applied our methodology to separate cirrus and cumulus clouds in atmospheric imagery approximated as additive contributions to the observed signal. We evaluated the accuracy of multilayer separation results using synthetic images where we know the truth. We showed that when cirrus clouds become optically thick and indistinguishable from cumulus clouds, accurate layer separation becomes unfeasible.

As different channels contain different information about clouds, we showed that incorporating information from all channels in a multichannel framework further improves multilayer separation results. Multichannel cloud layer separation consistently generates more accurate results than channel-by-channel cloud layer separation.

Our future research will be focused on extending our methodology to multi-angle framework, which is essential for a more accurate cloud layer separation. Since nearby objects have a larger parallax than more distant objects when observed from different angles, multi-angle information will help to better separate optically-thick lower convective clouds, residuals of which are noticeable in image $\mathbf{u}$ (Fig. 3(c), top), and low-oscillatory upper cirrus clouds.

APPENDIX A
DETAILS ON MULTILAYER SEPARATION OF SINGLE-CHANNEL IMAGES

As briefly described in Section III, we solve multilayer separation problem by sequentially solving scale separation, segmentation, and disocclusion subproblems. Details on solving each of these subproblems are presented in this appendix.

A. Scale Separation

We first solve the scale separation problem (2). There are a variety of choices for the norm $||\cdot||_*$ modeling high oscillatory components, including those known in the image processing literature as H^{-1}, BMO^{-1}, L^1, among others [10], [12], [13], [18]. The regularizing functional $R(u)$ can be in the form of bounded variation (BV) norm, measuring the total variation (TV), or can take the form of Besov norm. In particular, the BV norm, originally proposed for image denoising by [25], had since been used to solve a variety of problems in image processing and computer vision. The effectiveness of the BV norm stems from its ability to preserve edges in an image.

In our analysis, the choice of $R(u)$ is the total variation (TV), defined as

$$||u||_{\mathrm{TV}} = ||\nabla u||_1 = \sum_{(i,j)\in\Omega} ||\nabla u_{ij}||,$$

where $\nabla u_{ij} \in \mathbb{R}^2$ is the discrete gradient of u at pixel (i, j). Here, the choice of $||\cdot||_*$ is $||\cdot||_1$. Hence, minimization problem in (2) can be written explicitely as

$$\min_{\tilde{u}} \; \{ \; ||\nabla \tilde{u}||_1 + \mu ||f - \tilde{u}||_1 \; \} \, . \tag{7}$$

This formulation is related to problems that arise frequently in compressed sensing, where function u is reconstructed from a small subset of its Fourier coefficients [22], [23].

Alternating minimization algorithms, which are derived using variable-splitting techniques in optimization, were proposed in [26] for TV-L^1 deconvolution problems. In order to minimize (7), an additional variable $\mathbf{d} \in \mathbb{R}^2$ is introduced to transfer $\nabla \tilde{u}$ out of non-differentiable terms at each pixel, and

$ci = 0.8$, $cu = 0.965$, $ci/cu = 0.829$ $ci = 1.7$, $cu = 0.725$, $ci/cu = 2.345$ $ci = 2.3$, $cu = 0.350$, $ci/cu = 6.571$

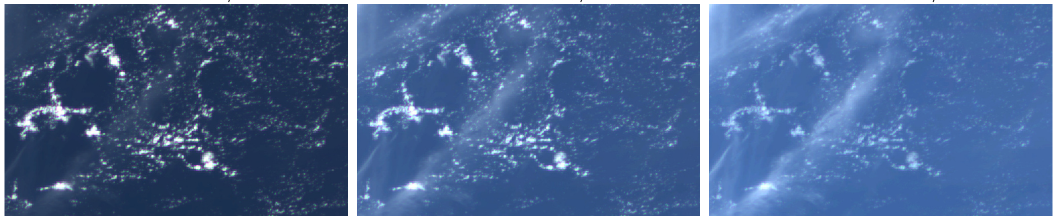

(a) Images $\mathbf{f}$ obtained by combining cirrus and cumulus clouds from Fig. 4(a,b) using different opaqueness coefficients.

(b) True cirrus cloud layers

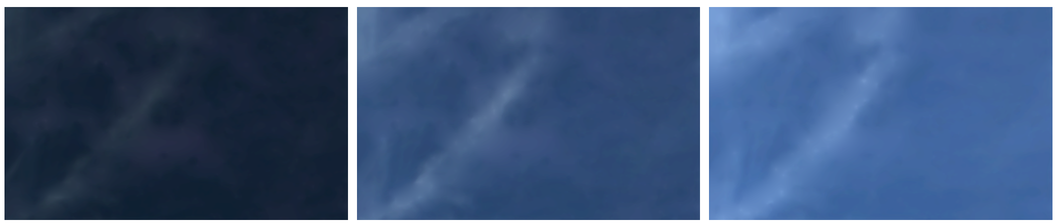

(c) Cirrus layers recovered by multichannel cloud layer separation

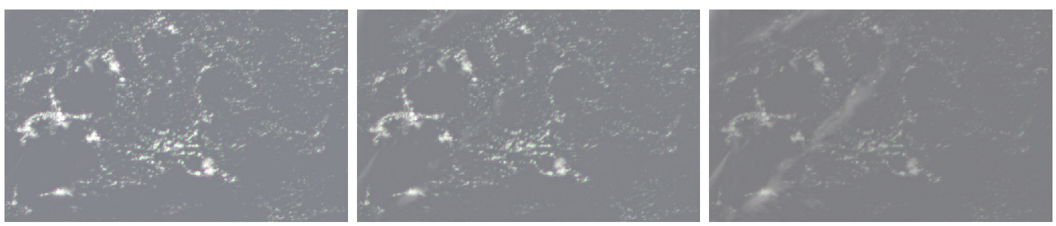

(d) Cumulus layers recovered by multichannel cloud layer separation

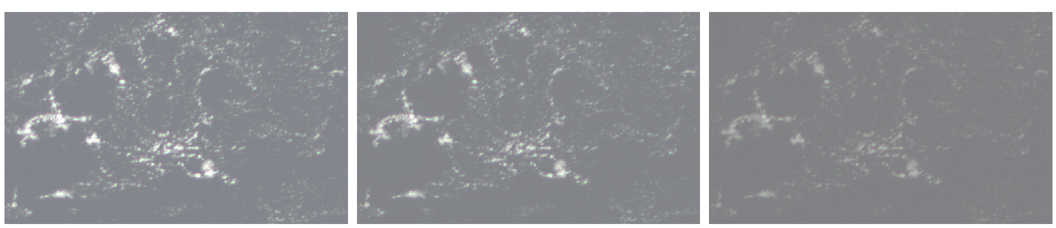

(e) True cumulus layers

Fig. 5. Multichannel cloud layer separation results for synthetically constructed images. (a) Images $\mathbf{f}$ obtained by combining cirrus and cumulus clouds from Fig. 4(a,b) using different opaqueness coefficients are shown. (b,e) Cirrus and cumulus layers that compose images in (a) are shown. (c,d) Cirrus and cumulus layers obtained using multichannel layer separation. The coefficients for the first column: $ci = 0.8$, $cu = 0.965$, $ci/cu = 0.829$; second column: $ci = 1.7$, $cu = 0.725$, $ci/cu = 2.345$; third column: $ci = 2.3$, $cu = 0.350$, $ci/cu = 6.571$.

$||\mathbf{d} - \nabla\tilde{u}||^2$ is penalized. Since L^1 term $||f - \tilde{u}||_1$ in equation (7) is not quadratic in $\tilde{u}$, an additional variable z is introduced to approximate $\tilde{u} - f$. Hence, we rewrite the minimization problem for (7) as

$$\min_{\tilde{u},\mathbf{d},z} \left\{ ||\mathbf{d}||_1 + \frac{\lambda}{2}||\mathbf{d} - \nabla\tilde{u}||^2 + \mu||z||_1 + \frac{\alpha}{2}||z - (\tilde{u} - f)||^2 \right\}, \tag{8}$$

where λ and α are nonnegative parameters.

For a fixed $\tilde{u}$, the minimization problems for $\mathbf{d}$ and z are

$$\mathbf{d}^* = \arg\min_{\mathbf{d}} \left\{ ||\mathbf{d}||_1 + \frac{\lambda}{2}||\mathbf{d} - \nabla\tilde{u}||^2 \right\}, \tag{9}$$
$$z^* = \arg\min_{z} \left\{ \mu||z||_1 + \frac{\alpha}{2}||z - (\tilde{u} - f)||^2 \right\},$$

which can be explicitly solved for $\mathbf{d}$ and z, at each pixel, by using a generalized and the one-dimensional shrinkage formulas, respectively [27], [28]:

$$\mathbf{d} \;=\; \max\left\{||\nabla\tilde{u}|| - \frac{1}{\lambda}, 0\right\}\frac{\nabla\tilde{u}}{||\nabla\tilde{u}||}, \tag{10}$$

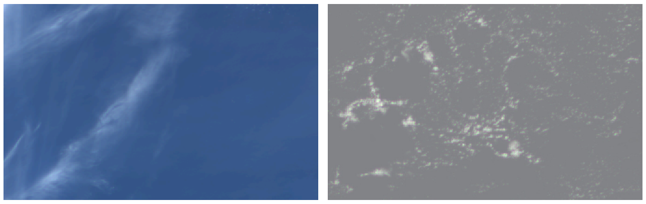

(a) True cirrus layer (left) and cumulus layer (right)

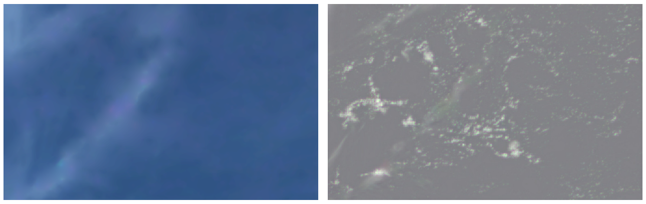

(b) Channel-by-channel cloud layer separation result

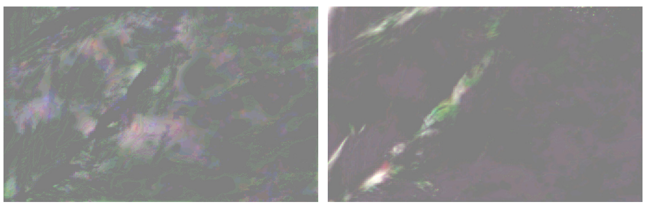

(c) Errors (magnified by a factor of 5) in channel-by-channel cloud layer separation result

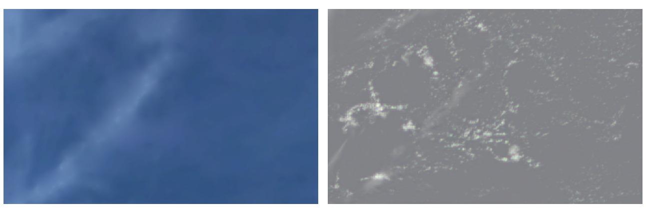

(d) Multichannel cloud layer separation result

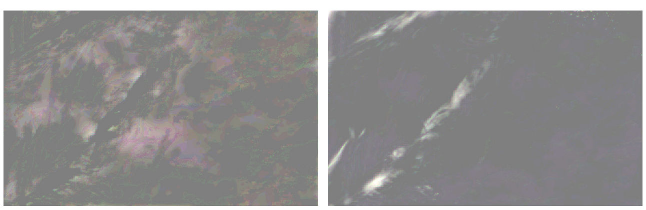

(e) Errors (magnified by a factor of 5) in multichannel cloud layer separation result

Fig. 6. Channel-by-channel and multichannel cloud layer separation of synthetic image in Fig. 4(c), with $ci/cu = 3.704$, into cirrus and cumulus layers. (a) The true layers are shown. (b) Channel-by-channel layer separation result and (c) corresponding errors (magnified by a factor of 5) are shown. Errors are the differences between computed result and the truth. (d) Multichannel layer separation result and (e) corresponding errors (magnified by a factor of 5) are shown.

$$z \;=\; \max\left\{|\tilde{u}-f| - \frac{\mu}{\alpha}, 0\right\} \operatorname{sign}(\tilde{u}-f).$$

For a fixed $\mathbf{d}$ and z, the minimization problem (8) is quadratic in $\tilde{u}$:

$$\tilde{u}^* \;=\; \arg\min_{\tilde{u}} \;\left\{ ||\mathbf{d}-\nabla\tilde{u}||^2 \;+\; \frac{\alpha}{\lambda}||z-(\tilde{u}-f)||^2 \right\},$$

and has the optimality condition:

$$(\alpha - \lambda\triangle)\,\tilde{u} = \alpha(f+z) - \lambda\nabla\cdot\mathbf{d},$$

which we solve using the fast Fourier transform.

In our experiment, the choice of parameters was: $\mu = 0.1$, $\lambda = 1.0$, and $\alpha = 1.0\mu$. The minimum and maximum intensity values for each image are 0 and 255, respectively.

See Fig. 1 (step 1) for an example of a result after scale separation was performed.

B. Segmentation

Scale separation, as described in Appendix A-A, generates only a rough estimate of multilayer separation. As seen on Fig. 1 (step 1), scale separation leaves traces of optically thick convective clouds in the image containing low-oscillatory cirrus layer. Such irregularities occur in the regions where optically thick lower convective clouds occupy large contiguous areas in the image. Our aim is to perform disocclusion only in these regions. However, we first need to find regions D or, equivalently, determine region boundaries ∂D. In order to find ∂D, we perform segmentation of image $\tilde{v}$ (see Fig. 1, step 2).

The segmentation can be achieved, for example, via solving the following minimization problem [21]:

$$\begin{aligned} F(a_1, a_2, \partial D) \;&=\; \gamma\int_{\partial D} ds \\ &\quad + \int_D (\tilde{v}(x,y) - a_1)^2\, dxdy \\ &\quad + \int_{\Omega\backslash D} (\tilde{v}(x,y) - a_2)^2\, dxdy, \end{aligned} \tag{11}$$

$$\min_{a_1, a_2, \partial D} F(a_1, a_2, \partial D),$$

where a_1 and a_2 are averages of $\tilde{v}$ inside and outside D, respectively. Minimizing the fitting error, which is represented by the last two terms in the energy functional (11), the model looks for the best segmentation of $\tilde{v}$ taking only two values, namely a_1 and a_2. The first term is the regularizer in the form of the length of the boundary ∂D, and $\gamma > 0$ is a parameter. Eq. (11) can be re-written using level set formulation [29], [30].

In our experiment, $\gamma = 0.001 \cdot 255^2$. See Fig. 1 (step 2) for an example of segmentation result.

C. Disocclusion

Disocclusion, an important inverse problem with many applications, is the process for reconstructing corrupted or obstructed parts of an image. Image disocclusion received considerable interest since the pioneering papers by [31], [32], who proposed variational principles for obtaining solutions to such problems.

Here, we use a different technique, based on fast operator splitting methods, to solve disocclusion problem. After determining region D in Appendix A-B, we can perform disocclusion to recover low-oscillatory layer u that is obstructed by opaque layer v. Similar to scale separation functional (2), we use $||u||_{TV}$ as regularizer for the disocclusion minimization problem (3), which can be written as

$$\begin{cases} \min\limits_u \;||\nabla u||_1 & \text{in } D, \\ u = \tilde{u} & \text{in } \Omega\backslash D, \end{cases} \tag{12}$$

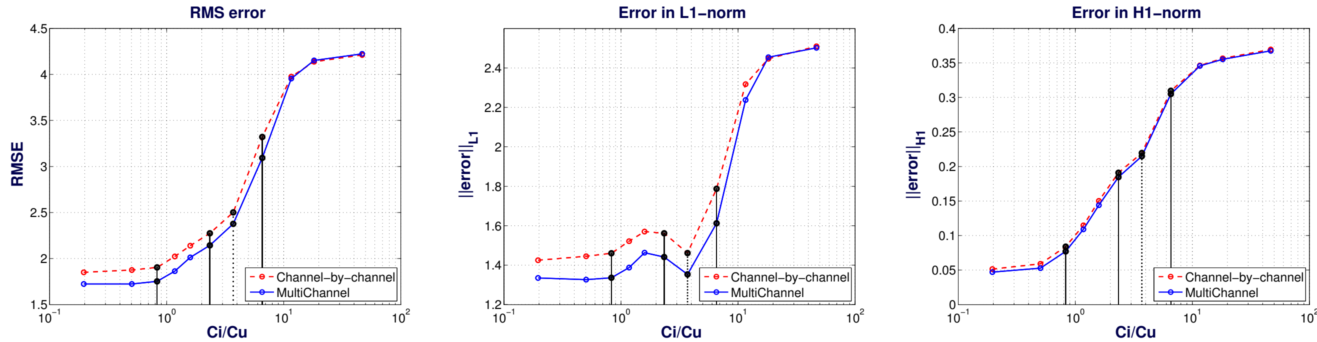

(a) RMS error (b) L_1-error (c) H_1-error

Fig. 7. RMS errors and errors in L_1-norm and H_1-norm between computed results and the truth for channel-by-channel and multichannel cloud layer separations for different ci/cu ratios are shown. The values marked with solid black vertical lines correspond to the cases studied on Fig. 5 and dashed line corresponds to the case of Fig. 6. For reference, the synthetic images were scaled to be between 0 and 255. See main text for more discussion.

with $u_0 = \tilde{u}$ as initial conditions and Neumann boundary conditions.

Fast operator-splitting and alternating minimization methods were proposed in [33], [34] for TV-L^2 deconvolution problem. Also, the Split Bregman method was proposed in [35] for solving TV-L^2 denoising problems. In these methods, and as in (8), variable $\mathbf{d}$ is introduced and $||\mathbf{d} - \nabla u||^2$ is penalized. Hence, we rewrite the minimization problem for (12) as

$$\min_{u,\mathbf{d}} \left\{ ||\mathbf{d}||_1 + \frac{\beta}{2}||\mathbf{d} - \nabla u||^2 \right\}, \tag{13}$$

where β is a nonnegative parameter. For a fixed u, the minimization problem for $\mathbf{d}$ and its solution are given by (9) and (10), respectively. For a fixed $\mathbf{d}$, the minimization problem (13) is quadratic in u, and the minimizer u^* is given by

$$u^* = \arg\min_u ||\mathbf{d} - \nabla u||^2,$$

which has the optimality condition:

$$\triangle u = \nabla \cdot \mathbf{d}.$$

In our experiment, $\beta = 0.18$. See Fig. 1 (step 3) for an example of result after disocclusion was performed.

Appendix B
Details on Multilayer Separation of Multichannel Images

The regularization term $R(\mathbf{u})$ in (4) and (5) is the multichannel total variation (MTV) [36], [37], defined as

$$\begin{aligned} ||\mathbf{u}||_{\mathrm{MTV}} &= ||\nabla \mathbf{u}||_1 \\ &= \sum_{(i,j)\in\Omega} \sqrt{||\nabla u_{ij}^{(1)}||^2 + ||\nabla u_{ij}^{(2)}||^2 + \ldots + ||\nabla u_{ij}^{(C)}||^2}. \end{aligned}$$

The norm $||\cdot||_*$ is $||\cdot||_1$. Hence, similar to (7) and (12), minimization problems for scale separation and disocclusion can be written as

$$\min_{\tilde{\mathbf{u}}} \; \{ \; ||\nabla \tilde{\mathbf{u}}||_1 + \mu ||\mathbf{f} - \tilde{\mathbf{u}}||_1 \; \}$$

and

$$\begin{cases} \min\limits_{\mathbf{u}} \; ||\nabla \mathbf{u}||_1 & \text{in } D, \\ \mathbf{u} = \tilde{\mathbf{u}} & \text{in } \Omega \backslash D, \end{cases}$$

respectively. The multichannel image segmentation method [38] can be used to determine locations of optically thick and high-oscillatory clouds:

$$\begin{aligned} F(\mathbf{a}_1, \mathbf{a}_2, \partial D) &= \gamma \int_{\partial D} ds \\ &+ \int_D \frac{1}{C} \sum_{c=1}^{C} (\tilde{v}^{(c)}(x,y) - a_1^{(c)})^2 \, dxdy \\ &+ \int_{\Omega \backslash D} \frac{1}{C} \sum_{c=1}^{C} (\tilde{v}^{(c)}(x,y) - a_2^{(c)})^2 \, dxdy, \end{aligned}$$

$$\min_{\mathbf{a}_1, \mathbf{a}_2, \partial D} F(\mathbf{a}_1, \mathbf{a}_2, \partial D),$$

where $\mathbf{a}_1 = (a_1^{(1)}, a_1^{(2)}, \ldots, a_1^{(C)})$ and $\mathbf{a}_2 = (a_2^{(1)}, a_2^{(2)}, \ldots, a_2^{(C)})$ are unknown constant vectors, representing averages of $\tilde{\mathbf{v}}$ inside and outside D, respectively.

Following such generalizations to notations for vector-value functions, equations for scale-separation, segmentation, and disocclusion in multichannel case are similar to those in single-channel case in Appendix A and are therefore omitted.

We consistently used the same set of parameters for all multichannel experiments. The values of the parameters are: $\mu = 0.05$, $\lambda = 1.0$, and $\alpha = 1.0\mu$ for scale separation, $\gamma = 0.001 \cdot 255^2$ for segmentation, and $\beta = 0.045$ for disocclusion. The minimum and maximum intensity values for each image are 0 and 255, respectively.

Acknowledgment

The work was largely supported by National Aeronautics and Space Administration, Earth Science Technology Office AIST-QRS-12-0003 Grant (3D-TRACE project). ABD also acknowledges support from NASA's SMD/ESD Radiation Sciences programs. IY is also thankful for the National Science Foundation Grant DMS 1217239. The research was carried out at the Jet Propulsion Laboratory, California Institute of Technology, under a contract with the National Aeronautics and Space Administration. The authors thank David Diner, Michael Garay, Veljko Jovanovic, Brian Rheingans, Luminita Vese, and Kevin Vixie for their helpful discussions and comments.

References

[1] B. Albrecht, "Aerosols, cloud microphysics, and fractional cloudiness," *Science*, vol. 245, no. 4923, pp. 1227–1230, 1989.

[2] S. Twomey, "Aerosols, clouds and radiation," *Atmospheric Environment A*, vol. 25, no. 11, pp. 2435–2442, 1991.

[3] V. Ramanathan, P. Crutzen, J. Kiehl, and D. Rosenfeld, "Aerosols, climate, and the hydrological cycle," *Science*, vol. 294, pp. 2119–2124, 2001.

[4] S. Bony and J.-L. Dufresne, "Marine boundary layer clouds at the heart of tropical cloud feedback uncertainties in climate models," *Geophysical Research Letters*, vol. 32, no. 20, 2005.

[5] J.-L. Dufresne and S. Bony, "An assessment of the primary sources of spread of global warming estimates from coupled atmosphere-ocean models," *Journal of Climate*, vol. 21, no. 19, pp. 5135–5144, 2008.

[6] IPCC, *Climate Change 2013: The Physical Science Basis. Summary for Policymakers*, T. Stocker, D. Qin, G.-K. Plattner, M. Tignor, S. Allen, J. Boschung, A. Nauels, Y. Xia, V. Bex, and P. Midgley, Eds. IPCC, Cambridge University Press, Cambridge, United Kingdom and New York, NY, USA, 2013.

[7] G. E. Thomas and K. Stamnes, *Radiative Transfer in the Atmosphere and Ocean*. Cambridge University Press, 2002.

[8] B.-C. Gao, A. F. H. Goetz, and W. J. Wiscombe, "Cirrus cloud detection from airborne imaging spectrometer data using the 1.38 μm water vapor band," *Geophys. Res. Lett.*, vol. 20, pp. 301–304, 1993.

[9] B.-C. Gao and Y. J. Kaufman, "Selection of 1.375-μm channel for remote sensing of cirrus clouds and stratospheric aerosols from space," *J. Atmos. Sci*, vol. 52, pp. 4231–4237, 1995.

[10] S. Alliney, "Digital filters as L1-norm regularizers," *Sixth Multidimensional Signal Processing Workshop*, p. 105, 1989.

[11] ——, "Digital filters as absolute norm regularizers," *IEEE Transactions on Signal Processing*, vol. 40, no. 6, pp. 1548–1562, 1992.

[12] Y. Meyer, *Oscillating patterns in image processing and nonlinear evolution equations*. Providence, RI: American Mathematical Society, 2001.

[13] S. Osher, A. Sole, and L. Vese, "Image denoising and decomposition with total variation minimization and oscillatory functions," *Multiscale Modeling & Simulation*, vol. 1, no. 3, pp. 349–370, 2003.

[14] M. Nikolova, "Minimizers of cost-functions involving nonsmooth data-fidelity terms. Application to the processing of outliers," *SIAM Journal on Numerical Analysis*, vol. 40, no. 3, pp. 965–994, 2003.

[15] ——, "A variational approach to remove outliers and impulse noise," *Journal of Mathematical Imaging and Vision*, vol. 20, pp. 99–120, 2004.

[16] T. Chan and S. Esedoglu, "Aspects of total variation regularized L1 function approximation," *SIAM Journal on Applied Mathematics*, vol. 65, no. 5, pp. 1817–1837, 2005.

[17] A. Buades, T. Le, J.-M. Morel, and L. Vese, "Fast cartoon + texture image filters," *IEEE Transactions on Image Processing*, vol. 19, no. 8, pp. 1978–1986, 2010.

[18] J. Garnett, P. Jones, T. Le, and L. Vese, "Modeling oscillatory components with the homogeneous spaces $B\dot{M}O^{-\alpha}$ and $\dot{W}^{-\alpha,p}$," *Pure and Applied Mathematics Quarterly*, vol. 7, no. 2, pp. 275–318, 2011.

[19] V. Caselles, R. Kimmel, and G. Sapiro, "Geodesic active contours," *International Journal of Computer Vision*, vol. 22, no. 1, pp. 61–79, 1997.

[20] S. Kichenassamy, A. Kumar, P. Olver, A. Tannenbaum, and A. Yezzi, "Conformal curvature flows: From phase transitions to active vision," *Archive for Rational Mechanics and Analysis*, vol. 134, no. 3, pp. 275–301, 1996.

[21] T. Chan and L. Vese, "Active contours without edges," *IEEE Transactions on Image Processing*, vol. 10, no. 2, pp. 266–277, 2001.

[22] E. Candes, J. Romberg, and T. Tao, "Robust uncertainty principles: Exact signal reconstruction from highly incomplete frequency information," *IEEE Transactions on Information Theory*, vol. 52, no. 2, pp. 489–509, 2006.

[23] D. Donoho, "Compressed sensing," *IEEE Transactions on Information Theory*, vol. 52, no. 4, pp. 1289–1306, 2006.

[24] D. Diner, J. Beckert, T. Reilly, C. Bruegge, J. Conel, R. Kahn, J. Martonchik, T. Ackerman, R. Davies, S. A. W. Gerstl, H. Gordon, J.-P. Muller, R. Myneni, P. Sellers, B. Pinty, and M. Verstraete, "Multi-angle Imaging SpectroRadiometer (MISR) instrument description and experiment overview," *IEEE Transactions on Geoscience and Remote Sensing*, vol. 36, no. 4, pp. 1072–1087, 1998.

[25] L. Rudin, S. Osher, and E. Fatemi, "Nonlinear total variation based noise removal algorithms," *Physica D*, vol. 60, pp. 259–268, 1992.

[26] J. Yang, Y. Zhang, and W. Yin, "An efficient TVL1 algorithm for deblurring multichannel images corrupted by impulsive noise," *SIAM J. Sci. Comput.*, vol. 31, no. 4, pp. 2842–2865, 2009.

[27] D. L. Donoho and I. M. Johnstone, "Adapting to unknown smoothness via wavelet shrinkage," *Journal of The American Statistical Association*, vol. 90, no. 432, pp. 1200–1224, 1995.

[28] Y. Wang, W. Yin, and Y. Zhang, "A fast algorithm for image deblurring with total variation regularization," *CAAM Technical Report*, vol. TR07-10, 2007.

[29] S. Osher and J. Sethian, "Fronts propagating with curvature dependent speed: Algorithms based on Hamilton-Jacobi formulations," *Journal of Computational Physics*, vol. 79, pp. 12–49, 1988.

[30] S. Osher and R. Fedkiw, *Level Set Methods and Dynamic Implicit Surfaces*, ser. Applied Mathematical Sciences. New York: Springer-Verlag, 2003.

[31] S. Masnou and J.-M. Morel, "Level lines based disocclusion," *International Conference on Image Processing*, vol. 3, pp. 259–263, 1998.

[32] S. Masnou, "Disocclusion: A variational approach using level lines," *IEEE Transactions on Image Processing*, vol. 11, no. 2, pp. 68–76, 2002.

[33] Y. Wang, J. Yang, W. Yin, and Y. Zhang, "A new alternating minimization algorithm for total variation image reconstruction," *SIAM J. Imaging Sci.*, vol. 1, no. 3, pp. 248–272, 2008.

[34] J. Yang, W. Yin, Y. Zhang, and Y. Wang, "A fast algorithm for edge-preserving variational multichannel image restoration," *SIAM J. Imaging Sci.*, vol. 2, pp. 569–592, 2009.

[35] T. Goldstein and S. Osher, "The split bregman method for L1-regularized problems," *SIAM J. Imaging Sci.*, vol. 2, no. 2, pp. 323–343, 2009.

[36] G. Aubert and P. Kornprobst, *Mathematical Problems in Image Processing: Partial Differential Equations and the Calculus of Variations*, ser. Applied Mathematical Sciences. New York: Springer-Verlag, 2006, vol. 147.

[37] D. Tschumperle and R. Deriche, "Vector-valued image regularization with PDEs: A common framework for different applications," *IEEE Transactions on Pattern Analysis and Machine Intelligence*, vol. 27, no. 4, pp. 506–517, 2005.

[38] T. Chan, B. Sandberg, and L. Vese, "Active contours without edges for vector-valued images," *Journal of Visual Communication and Image Representation*, vol. 11, no. 2, pp. 130–141, 2000.

Igor Yanovsky received the B.S. and the M.S. degrees both in applied mathematics from the University of California, Los Angeles in 2002, and the Ph.D. in applied mathematics from the University of California, Los Angeles in 2008. Igor joined the Jet Propulsion Laboratory, California Institute of Technology in 2008. His research interests are inverse problems and data analysis particularly in areas of remote sensing, signal and image processing, computer vision, medical imaging, and atmospheric sciences.

Anthony B. Davis (BSc, Physics, U. Paris VI 1977; MSc, Physics, U. de Montréal 1982; PhD, Physics, McGill 1992) has worked remote sensing problems for over two decades successively at NASA's Goddard Space Flight Center in Greenbelt, Maryland, DOE's Los Alamos National Laboratory in New Mexico, and now at the Jet Propulsion Laboratory in Pasadena, CA. His main focus has been on cloud remote sensing and the related problem of how clouds impact the Earth's radiative energy budget. He specializes in the challenges posed by the 3D shapes of real clouds to which he brings to bear his expertise in theoretical and computational vector radiative transfer for a physics-based prediction of the spectral and/or polarimetric signals from clouds as measured by ground-, aircraft- and space-based sensors using both passive (solar/thermal) and active (pulsed laser source) modalities. Since his arrival at JPL in 2009, his interests have grown to include aerosol/surface property retrievals, as well as column-integrated amounts of green house gases such as CO_2, particularly in the vicinity of clouds, or in other spatially complex situations, using multi-pixel/multi-angle spectral data with or without polarization diversity.